Annals of Nuclear Energy 192 (2023) 109991

Contents lists available at ScienceDirect

Annals of Nuclear Energy

journal homepage: www.elsevier.com/locate/anucene

Effects of angles and shapes of a corner crack on the driving force at a set-in nozzle-cylinder in a PWR pressure vessel

Shuai Wang [a,b,c], Bin Wang [b,*], Guiyi Wu [c,*], He Xue [d], Yuman Sun [d], Jiajun Zhu [d]

[a] School of Safety Science and Engineering, Xi'an University of Science and Technology, Xi'an 710054, China
[b] Department of Mechanical and Aerospace Engineering, Brunel University, London UB8 3PH, UK
[c] Centre of Excellence for Advanced Materials, Dongguan 523808, China
[d] School of Mechanical Engineering, Xi'an University of Science and Technology, Xi'an 710054, China

ARTICLE INFO

Keywords:
Corner crack
Stress intensity factor (SIF)
J-integral
Reactor pressure vessel (RPV)
Elastic-plastic finite element analysis (EPFEA)

ABSTRACT

Corner cracks are one of the common forms of flaws in the reactor pressure vessels (RPVs) of nuclear power plants (NPPs). Accurate evaluation of the driving force of such corner cracks is essential and critical for the efficient design and integrity assessment of the RPVs. In this study, the combined effect of the depth, length and angle of a given corner crack under the service loading was analyzed using elastic–plastic finite element analysis (EPFEA). Based on the consideration of the distribution profiles of stress intensity factor (SIF) and *J* integral as the crack growth along corner crack front, the crack growth stability with various crack shapes and angles was analyzed. Finite element analysis (FEA) results showed that the crack growth driving force is affected by the shape and angle of the initial crack. It is also found that the sliding mode (mode II) crack or tearing mode (mode III) crack should be taken into account in the structural integrity analysis of RPVs.

1. Introduction

Reactor pressure vessel (RPV) is one of the important components of primary coolant boundary, which is commonly used in the pressurized water reactors (PWRs) (Liu et al., 2020). This critical component operates under harsh working environment, such as high temperature, high pressure and neutron irradiation (Murtaza and Hyder, 2015a). The service-induced defects (cracks) are inevitable during the design life because of the stress concentration and irradiation embrittlement at the nozzle-cylinder intersection zone, and previous studies have shown that the corner crack initiated at set-in nozzle-cylinder of RPV is one of typical failure forms of RPVs (Murtaza and Hyder, 2017; Liu et al., 2021). As RPV is considered irreplaceable, the fracture analysis and assessment of the key locations in RPVs are thus required to ensure adequate safety margins to be maintained during operation (Liu et al., 2018).

To ensure the structural integrity of RPVs with cracks, substantial research has been carried out on corner cracks subjected to complex loading conditions. One of the earliest studies investigating the SIF of corner cracks using finite element analysis (FEA) was carried out by Ruiz in the 1970 s (Ruiz, 1973). Murtaza and Hyder performed the fracture mechanics analysis for the corner crack at the set-in nozzle of a reactor pressure vessel, they demonstrated that the corner crack with the depth of 5% of wall thickness is the critical crack at the nozzle-cylinder intersection of the RPV (Murtaza and Hyder, 2015b). The 1/4 wall thickness corner crack extension analysis at in-let nozzle of RPV of type AP1000 under design loading condition was completed by Liu et al. (2018), who showed that the crack growth rate of the nodes in the vicinity of RPV's inner surface is faster than that of the nodes in the centre area of crack front (Liu et al., 2018). Jin et al.(2019) studied the Weibull stress in the local approach to fracture for corner crack in RPVs, and found that the modified boundary layer model can effectively predict the Weibull stress along the crack tip (Jin et al., 2019). The influence of primary internal pressure and secondary thermal stress on the stress field at nozzle corner and SIF at crack front were analyzed by Li et al. (2020). They found that the corner crack size and shape affected the SIF value along the crack front, as well as the final critical crack size (Li et al., 2020). A fracture mechanics analysis procedure based on the review results of several technical codes and standards such as ASME B&PV Code, Sec.XI, was proposed by Kim et al. (2022), to evaluate structural integrity of PWR with corner cracks at the various nozzles. They pointed out that the axial corner crack in the RPV outlet nozzle has the stress intensity factor (SIF) exceeding the low bound of upper-shelf fracture toughness irrespectively of considering the constraint effect, but the *J*-integral for the axial crack of the outlet nozzle does not exceed

* Corresponding authors.
E-mail addresses: bin.wang@brunel.ac.uk (B. Wang), guiyi.wu@ceamat.com (G. Wu).

https://doi.org/10.1016/j.anucene.2023.109991
Received 4 October 2022; Received in revised form 6 June 2023; Accepted 14 June 2023
Available online 26 June 2023

Nomenclature

a	crack depth
c	crack length
ρ	density
σ_0	yield strength
σ_b	tensile strength
E	Young's modulus
ν	Poisson's ratio
ε	strain
φ	crack angle
J	J integral
K	stress intensity factor
g	gravitational acceleration
K_I	opening mode crack (mode I)
K_{II}	sliding mode crack (mode II)
K_{III}	tearing mode crack (mode III)
K_{max}	the maxima stress intensity converted from J integral
J_{max}	the maxima J integral value
K_{eff}	the effective linear elastic stress intensity factor in mixed mode loading
K_{12}	the fracture toughness at the initiation of ductile tearing
K_{mat}	the material fracture toughness measured by stress intensity factor
α	the parameter used in defining K_{eff}

Abbreviations

FEA	finite element analysis
SIF	stress intensity factor
RPV	reactor pressure vessel
NPP	nuclear power plant

Table 1
Chemical composition of SA508 steel (%).

C	Si	Mn	P	S	Cu	Mo	Cr	Ni	Fe
0.187	0.18	1.35	0.009	0.003	0.02	0.49	0.12	0.75	Bal.

Table 2
Mechanical properties of SA508 steel at 350 °C.

Young's modulus, E	Yield stress, $\sigma_{0.2}$	Tensile stress, σ_b	Poisson's ratio, ν	Density, ρ
214 GPa	415.6 MPa	577.1 MPa	0.3	7.75×10^{-9} tone/mm^3

the ductile crack initiation toughness (Kim et al., 2022). Previous studies have demonstrated that the crack tip opening displacement (CTOD), J-integral, and stress intensity factor (SIF) as the fracture parameters in structural integrity assessment (Qibao et al., 2022; Thamaraiselvi and Vishnuvardhan, 2020; Wang et al., 2023). It is generally accepted that the SIF around the corner crack front normally accurately evaluates the fracture conditions, which is relevant to the sizes and shapes of the crack and the geometric characteristics of the micro-level region around the crack front.

More recently, the corner crack growth was analysed numerically to predict the crack growing path. For instance, Sun et al. (2017, 2019) investigated the crack propagation path of the nozzle corner cracks under pressurized thermal shock loading by using XFEM combined with specified damage criterion. The results of the elastic and elastoplastic analysis showed that the axial crack propagation occurred prior to the radial crack propagation (Sun et al., 2017, Sun et al., 2019). Liu et al. (2020) studied the effects of thermal stress on the crack propagation in AP1000 RPV. They concluded that the type I crack has the greatest influence in the process of corner crack growth, and the type I crack has the greatest influence on the crack life (Liu et al., 2020). Any crack growth was assumed to happen by extending the crack length (or depth) but maintaining the same crack angles (i.e. vertical direction) in previous studies. However, pressurized RPV may be in biaxial or multi-axial loading conditions in reality, and the corner crack may change its angles under the mixed mode loading conditions (Wang et al., 2022). So far, most of studies investigated surface and corner cracks concentrating on mode I loading conditions, but there are still uncertainties in the effect of the mixed mode loading conditions on the shift of the SIF or J location along its crack front. To further understand the link between the crack

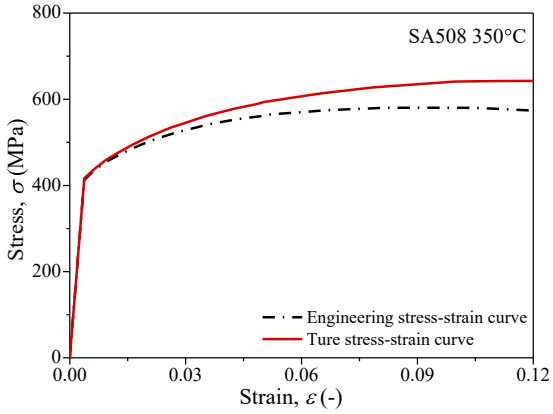

Fig. 1. The stress–strain curve derived from tensile tests of SA508 steel at 350 °C.

shape, angle, and the crack growth driving force, a more thorough investigation into the SIF or J along the corner crack of RPV will be beneficial. This study has looked into detailed profiles of the crack driving force along the whole crack front of a corner crack, including its deepest point and surface points, as well as the point of the maximum K and J, which could move between the deepest point and the surface points.

2. Finite element analysis

2.1. Material model

SA508 nuclear-grade steel has been used as the material of RPV in NPPs due to its strength, good ductility, low cost and good neutron irradiation resistance (Okonkwo et al., 2021). The chemical compositions of the material are shown in Table 1 (Dong et al., 2018).

350 °C is the design temperature of the RPVs, so the mechanical properties of the material at 350 °C were used in the numerical analyses. Details are listed in Table 2 (Murtaza and Hyder, 2017; Tian et al.,

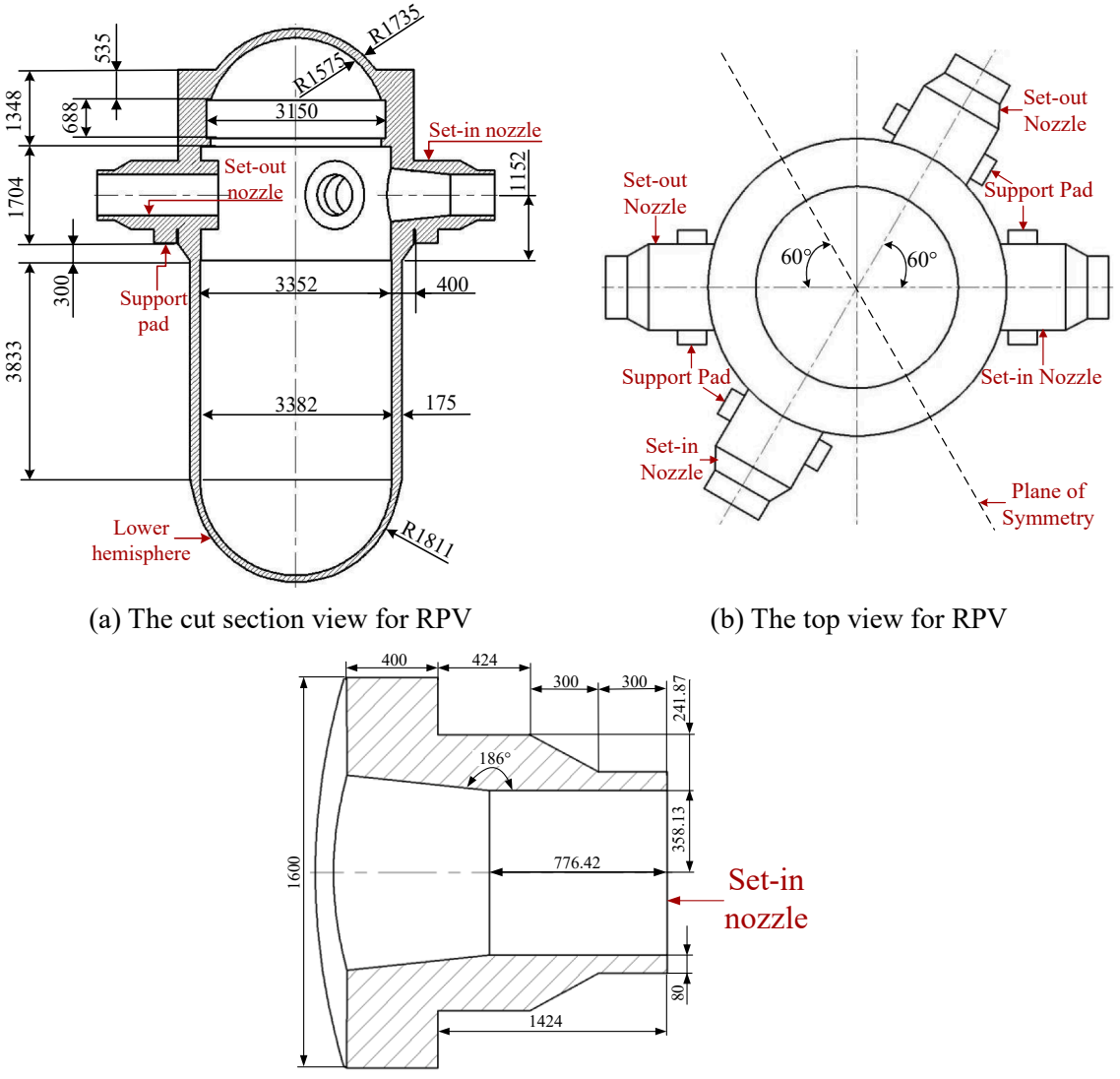

(a) The cut section view for RPV

(b) The top view for RPV

(c) The set-in nozzle with dimension parameters

Fig. 2. The cut section view for RPV and the set-in nozzle.

Table 3
Parameters of the corner crack.

No.	S-01	S-02	S-03
a	100 mm	200 mm	100 mm
c	200 mm	100 mm	100 mm
φ	−75°, −60°, −45°, −30°, −15°, 0°, 15°, 30°, 45°, 60°, 75°		

2020).

The plastic characteristics of SA508 steel at high temperature were investigated by a previous study using a uniaxial tensile test, with the mechanical response of SA508 steel at 350 °C showing in Fig. 1. The true stress–strain curve calculated from the uniaxial tensile test (i.e. engineering stress–strain curve) was used as the plastic parameters in the simulation process. To simplify the problem, the set-in (out) cylinder is assumed to be made of parent material (i.e. SA508) without weld and cladding.

2.2. Geometric model

A typical double-loop cylindrical 3D RPV model with two set-in and two set-out nozzles was analysed using ABAQUS (ABAQUS/Standard User's Manual, 2018). The cut section view for RPV and the set-in nozzle with dimension parameters are shown in Fig. 2 (a) to (c).

A symmetric model with a corner crack of the RPV was analysed using the sub-model technique with a refined mesh based on interpolation of the solution from an initial relatively coarse global model. This is to obtain an accurate, detailed solution in the crack region for the strain field and the stress intensity factor (K) as well as J integral (J) along the crack tip (Wang et al., 2021).

Different geometric parameters and angles of the corner crack were studied with different dimensions of cracks for a better understanding of crack driving force. Details are given in Table 3. These crack types have been classified in terms of the crack depth a, crack length c and crack angle φ, respectively.

It should be mentioned that φ is the angle of corner crack to the vertical direction, as show in Fig. 3. For convenience, the crack driving force along the crack tip will be normalized from point "A" to "B" shown in Fig. 3.

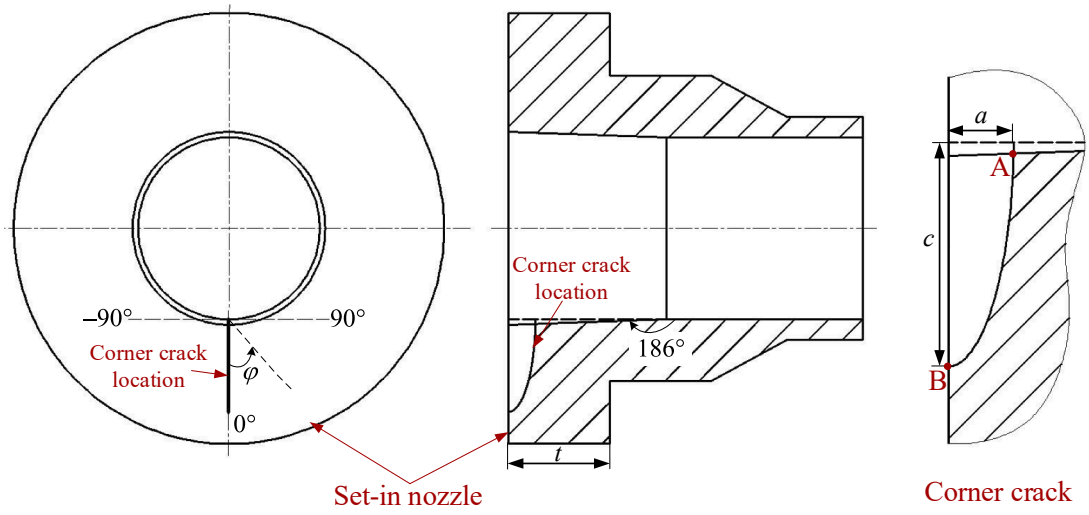

Fig. 3. Location of the corner crack and crack geometrical parameters.

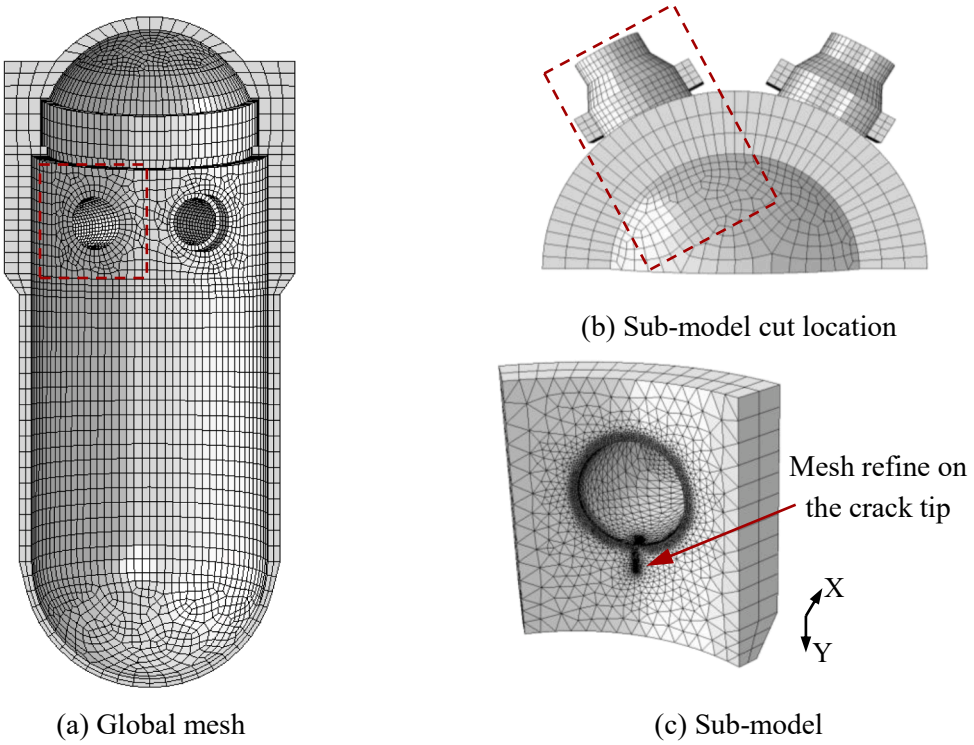

Fig. 4. Mesh model of RPV.

2.3. Boundary conditions

Owing to the use of metal materials and the huge size, the weight of RPV cannot be neglected. In the analysis, gravitational acceleration has been considered, gravitational acceleration $g = 9.8 \times 10^3 mm/s^2$. The RPV was supported by "support pads" under the nozzles in NPPs as shown in Fig. 2 (a) and (b). The lower face of these support pads was constrained on the vertical direction while the movement in the radial and tangential directions of these faces were allowed (i.e. the support pads were free to move in the axial direction of the nozzle). To properly support the RPV, as shown in Fig. 2 (a), the skirt type support was positioned under the lower hemisphere of the RPV. To incorporate the effects of skirt support, the lower hemisphere of the RPV was fixed in this study. The internal pressure of the RPV was set as 17.16 MPa, which is the design pressure of the RPV (Murtaza and Hyder, 2017).

2.4. The mesh and element choice

The mesh of the model is shown in Fig. 4, where the X-axis is the crack growth in the depth direction, and the Y-axis is the crack growth in the length direction.

The sub-model cut location from global mesh is shown in the red dashed box in Fig. 4 (a) and (b). Elements used in the global model are C3D8 (8-node quadratic brick) provided by ABAQUS, and the sub model with refined mesh on the tip of corner crack are C3D20 (20-node quadratic brick) provided by Franc 3D. The final global model and the sub-model have 8128 and 34,594 elements, respectively. The $M-$integral method was used to determine the K and J along the crack

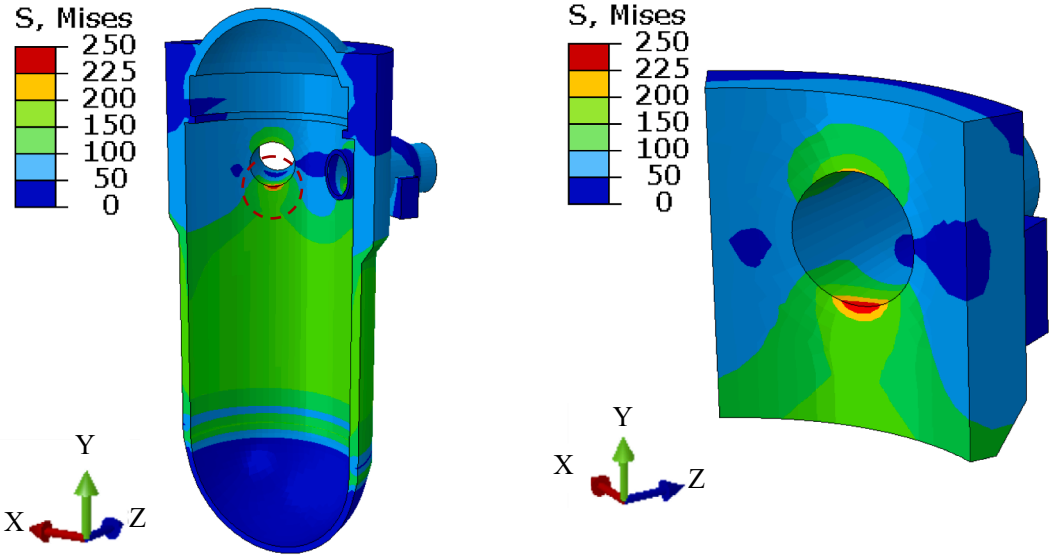

Fig. 5. The stress distributions of the uncracked RPV(MPa).

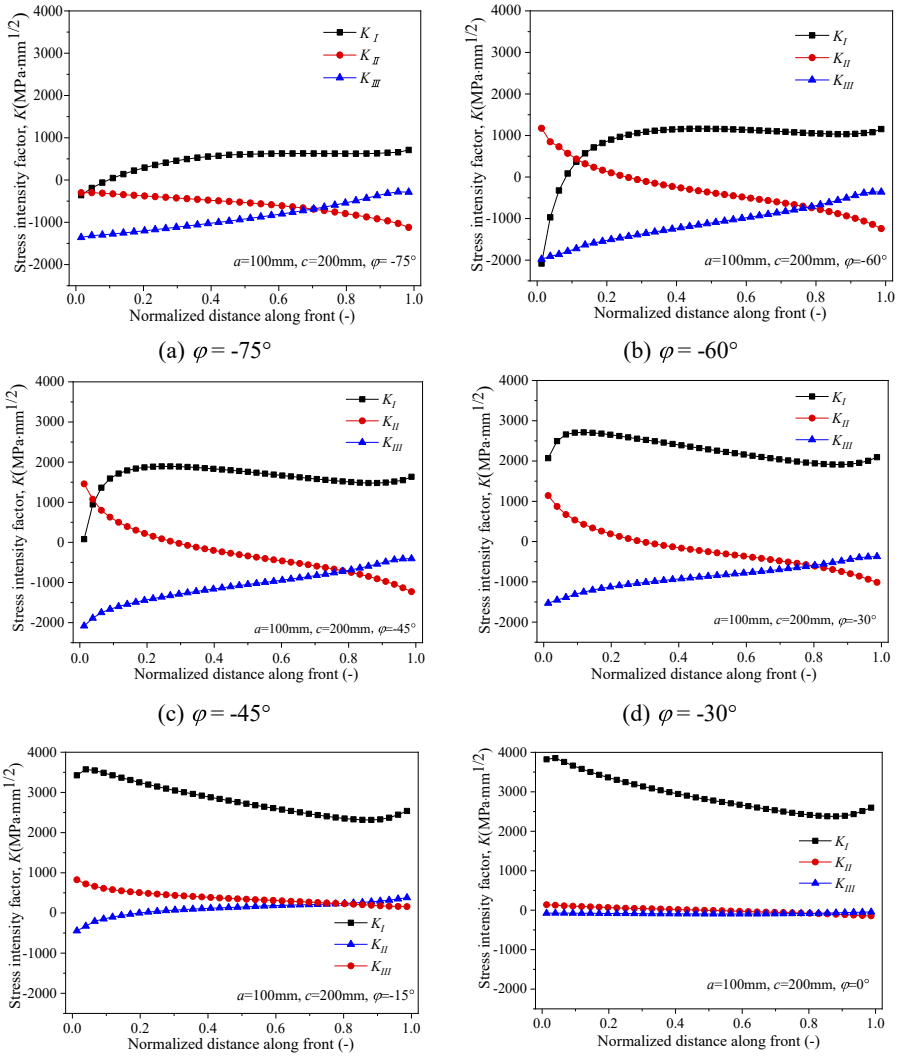

Fig. 6. Results of stress intensity factor for S-01 (a = 100, c = 200).

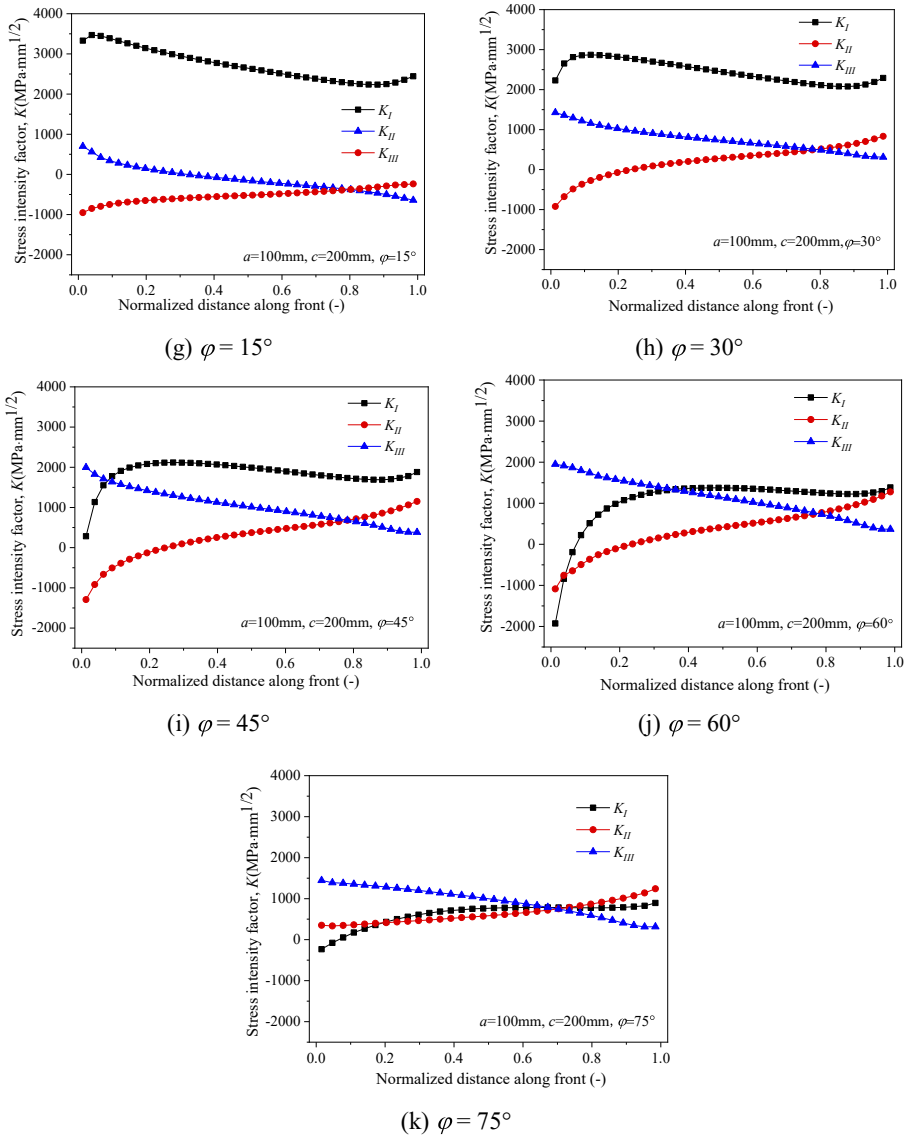

(g) $\varphi = 15°$ (h) $\varphi = 30°$

(i) $\varphi = 45°$ (j) $\varphi = 60°$

(k) $\varphi = 75°$

Fig. 6. (*continued*).

front (Zhang et al., 2017).

3. Simulation results and analyses

3.1. The stress analysis of the RPV

The stress distributions of the uncracked RPV are shown in Fig. 5 (a) and (b). Under identical internal pressure conditions, the cylinder with a larger wall thickness experiences higher stresses, resulting in a stress gap between the cylinder and the hemispherical bottom. The results show the highest stress concentration point being formed at the intersection area between the set-in nozzle-cylinder and the inner wall of the RPV. The maximum von Mises stress is 250.03 MPa, which is approximately in agreement with the results observed by Usman et al (Murtaza and Hyder, 2017).

3.2. The SIF from FEA

3.2.1. SIF of the corner cracks of set No.S-01 (a = 10 mm, c = 200 mm)

Fig. 6 (a) to (k) show the calculated value of the K along the whole crack front with a fixed depth and length (a = 100 mm, c = 200 mm) with different corner crack angles. The M integral was first introduced by Yau et al. (Yau et al., 1980) for mixed mode crack analysis in isotropic material. In this study, we use Franc 3D software to calculate J, K_I, K_{II} and K_{III}, the detailed calculations and theoretical basis are derived from the study of Banks-Sills et al. (Banks-Sills et al., 2005, 2007). The normalized distance along front is introduced to define the crack front from point "A" to "B" in Fig. 3. It can be seen that the distribution of K_I is higher than K_{II} and K_{III} in most cases, except for the K near the point "A" in some cases. In Fig. 6 (b) and (c), the K_{II} is apparently higher than K_I at the depth direction (near the point "A") of corner crack when the corner crack angles are −60° and −45°. In Fig. 6 (i) to (k), the K_{III} is higher than K_I at the depth direction of corner crack when the corner crack angle is greater than 45°. This suggests that the slant corner crack in RPV with complex stress condition are not only affected by tensile mode crack (mode I), but also influenced by sliding mode crack (mode II) or tearing mode crack (mode III). Hence, K_{II} and K_{III} should be take into account in the structural integrity analysis of RPV. It should be noted that the distribution of K_I seems to be approximately symmetric based on the symmetry axis of vertical corner crack (φ 0°), and K_{II} and K_{III} profile show the opposite trend.

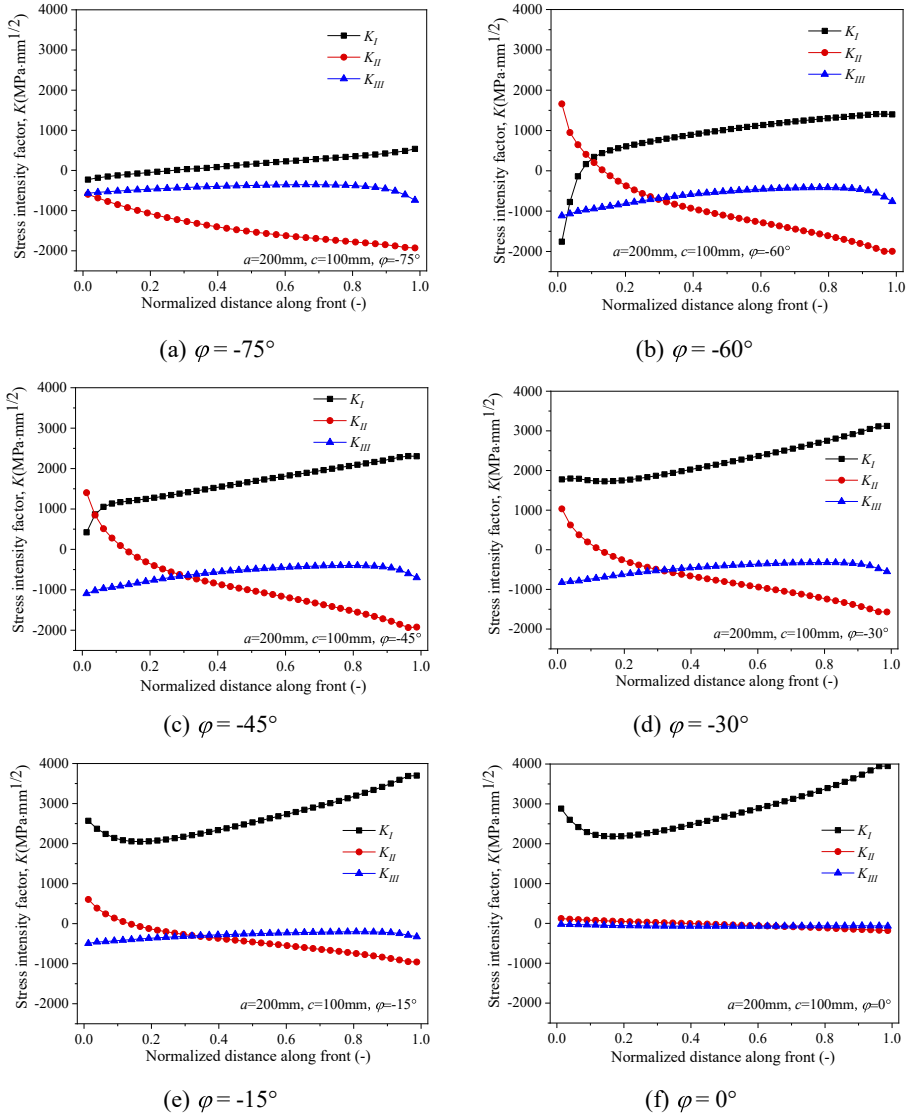

(a) $\varphi = -75°$ (b) $\varphi = -60°$

(c) $\varphi = -45°$ (d) $\varphi = -30°$

(e) $\varphi = -15°$ (f) $\varphi = 0°$

Fig. 7. Results of stress intensity factor for S-02 ($a = 200$, $c = 100$).

3.2.2. SIF of the corner cracks of set No.S-02 ($a = 200$, $c = 100$).

Compared with Fig. 6, Fig. 7 (a) to (k) show the calculated value of the K with a fixed depth and length ($a = 200$ mm, $c = 100$ mm) with respect to different corner crack angles. As the corner crack angle increases (or decreases) from the vertical direction ($\varphi = 0°$), the values of K_I, K_{II} and K_{III} change with the similar rule. In Fig. 7 (b) and (c), K_{II} is apparently higher than K_I at the depth direction (near the point "A") of corner crack when the corner crack angles are $-60°$ and $-45°$. In Fig. 7 (j) and 7 (k), the K_{III} is higher than K_I at the depth direction (near the point "A"). It should be noted that K_{II} is apparently higher than K_I along the whole crack front in Fig. 7 (k). This is very different from that in Fig. 6 (k), and it also reveals that sliding mode crack (mode II) should be take into account for the approximate horizontal corner crack ($\varphi = 75°$).

3.2.3. SIF of the corner cracks of set No.S-03 ($a = 100$, $c = 100$).

Fig. 8 (a) to (k) show the calculated value of the K with a fixed depth and length for a round corner crack ($a = 100$ mm, $c = 100$ mm) with respect to different angles. Compared with Fig. 7, Fig. 8 (a) to (k) shows the similar trends of K distribution. A key difference to Fig. 7 is that the K_I profile changes from convex (upside down U) with a single minimum at crack centre to two maxima near the ends when the corner crack angles from $-15°$ to $15°$, and the K_I profile are substantially symmetric in these cases. For the vertical round corner crack, the K_I at the deepest point is smaller than the surface point, which is in agreement with the results observed by Li et al (Li et al., 2020).

3.3. The J from FEA

The J integral, as the driving force of a crack, represents the potential or likelihood of the crack growth in elastoplastic materials. Figs. 9 to 11 shows the calculated values of J integral along the whole corner crack front. It can be easily seen that the J profile exhibits a maximum at the ends on the set-in nozzle (point "A") when corner crack angles are $\pm 60°$ for all cases. It is interesting to see that the trend of J profile for set No.S-01 and No.S-02 are approximately opposite in some cases (except angles of $\pm 60°$).

For round corner crack in Fig. 11, the J profile shows a symmetric upside down U shape distribution except the corner crack angles are $\pm 45°$and $\pm 60°$.

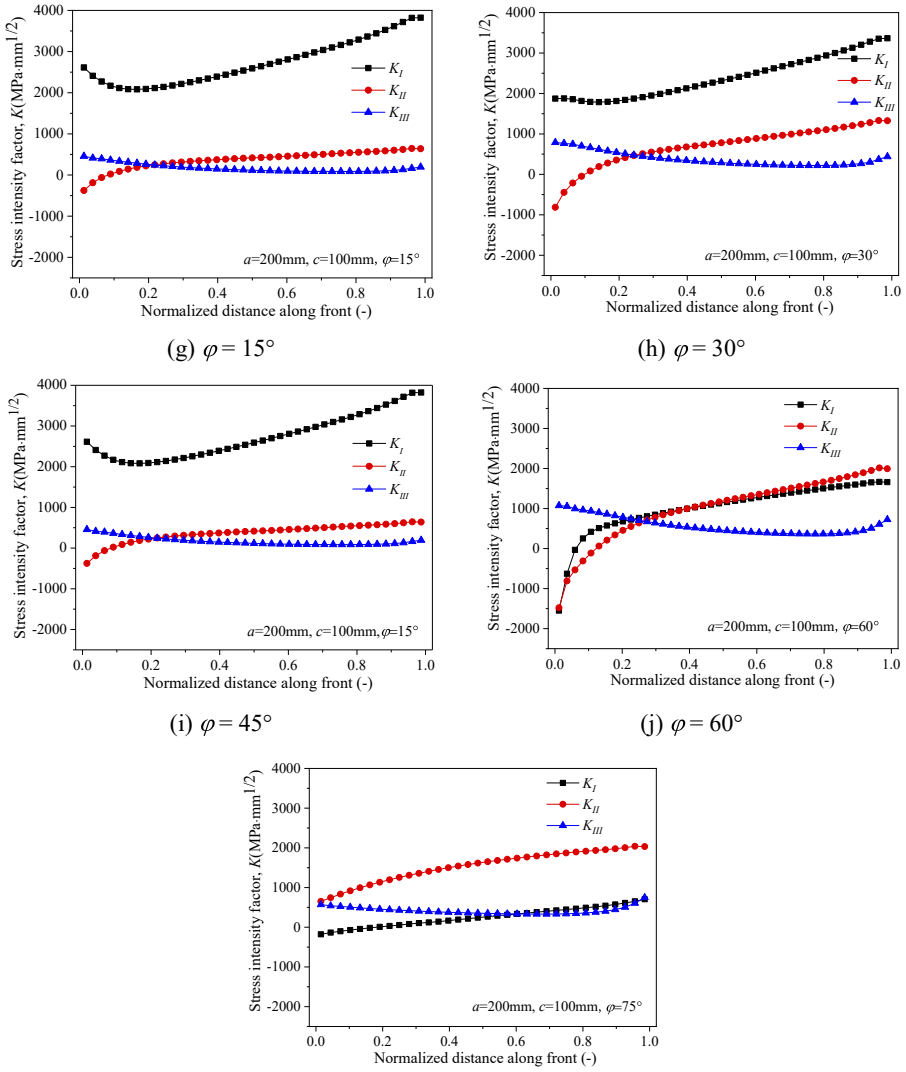

(g) $\varphi = 15°$ (h) $\varphi = 30°$

(i) $\varphi = 45°$ (j) $\varphi = 60°$

Fig. 7. (*continued*).

3.4. The maximum SIF or J from FEA

To further compare the trends of K and J integral from FEA, the maxima K and J with respect to the crack angles were studied. The relationship between maximum K, J, φ and crack shape are shown in Fig. 12. It can be seen that the maxima K and J profile shows similar variation trend in all cases. The K_I exhibits symmetric minimum values when the corner cracks are at $\pm 75°$, then gradually increases in value in a concave way (upside down U-shaped), reaching the maximum when the crack is vertical ($\varphi = 0°$). The K_{II} shows a local minimum value when the corner crack is at $-75°$, then gradually increases, reaching a local maximum value when the corner crack is at $-45°$ or $-60°$, and decrease to the local minimum when the crack is vertical ($\varphi = 0°$), then increase again, reaching a local maximum value when the corner crack is 75° (N-shape). The K_{III} shows a local minimum when the corner crack is at $-75°$, then gradually increases as the angle increases, reaching a local maximum when the corner crack is at $-45°$, and ultimately decreases slightly (S-shape). The change of the maximum K value appears to indicate that the opening mode crack (mode I) occupies the main position for crack growth when the corner crack is vertical, but when the crack angle gradually increases, the fracture mode tends to be sliding mode (mode II) or tearing mode (mode III) which are shown in specific cases (φ=±60°and $\varphi = 75°$).

To evaluate the crack under combinations of mode I, mode II and mode III loads, the effective linear elastic stress intensity factor in mixed mode loading K_{eff} was proposed in industrial codes and standards, such as R6 (British Energy, 2001) and BS7910 (BS7910:2019, 2019). The K_{eff} at the crack tip is given as.

If

$$\frac{K_{mat}}{\sigma_{0.2}} \geqslant 6.3\text{mm}^{1/2} \tag{1}$$

$$K_{eff}\left[K_{/}^{2} + K_{//}^{2} + \alpha K_{///}^{2}/(1-\text{n})\right]^{1/2} \tag{2}$$

If

$$\frac{K_{mat}}{\sigma_{0.2}} < 6.3\text{mm}^{1/2} \tag{3}$$

$$K_{eff}\left[K_{12}^{2} + \alpha K_{///}^{2}/(1-\text{n})\right]^{1/2} \tag{4}$$

where K_{mat} is the material fracture toughness measured by stress intensity factor, $\sigma_{0.2}$ the yield stress and ν the Poisson's ratio. Fracture toughness at initiation of ductile tearing K_{12} is given as (BS7910:2019, 2019)

$$K_{12}=\begin{cases}\dfrac{\left(2K_I+6\sqrt{K_I^2+8K_{II}^2}\right)}{8}\left(\dfrac{K_I^2+12K_{II}^2+K_I\sqrt{K_I^2+8K_{II}^2}}{2K_I^2+18K_{II}^2}\right)^{3/2}, & (|K_I/K_{II}|\geqslant 0.466)\\ \dfrac{|K_{II}|}{0.7}, & (|K_I/K_{II}|\langle 0.466)\end{cases} \tag{5}$$

It is conservative to set α 1 (BS7910:2019, 2019).

For SA508 steel, the K_{mat} under high temperature (320 °C) were tested by Li et al (Li et al., 2018), they found that the value of K_{mat} is approximately 210 MPa·m$^{1/2}$(≈6.6 × 10^3 MPa·mm$^{1/2}$). It is obtained that $\frac{K_{mat}}{\sigma_{0.2}}=15.9\text{mm}^{1/2}$, so K_{eff} can be calculated by Equation (2).

The maxima K_{eff} distribution profiles are shown in Fig. 12 in magenta solid line. The maxima K_{eff} is apparently higher than the maxima K_1 when the crack angle approaches to the horizontal direction, but roughly equals to K_1 when the crack is vertical. It reveals that the vertical corner crack has the great potential to propagate if the elastic SIF is used to characterize the crack driving force.

In Fig. 12 (a) to (c), there is a significant difference between the trends of K and J results. The J (red dash line) exhibits a symmetric local minimum value when the corner crack is ± 75°, then jumps to the approximately symmetric maximum value when the corner crack is ±60°, and then decreases with a sudden cliff-typed drop. The maxima J

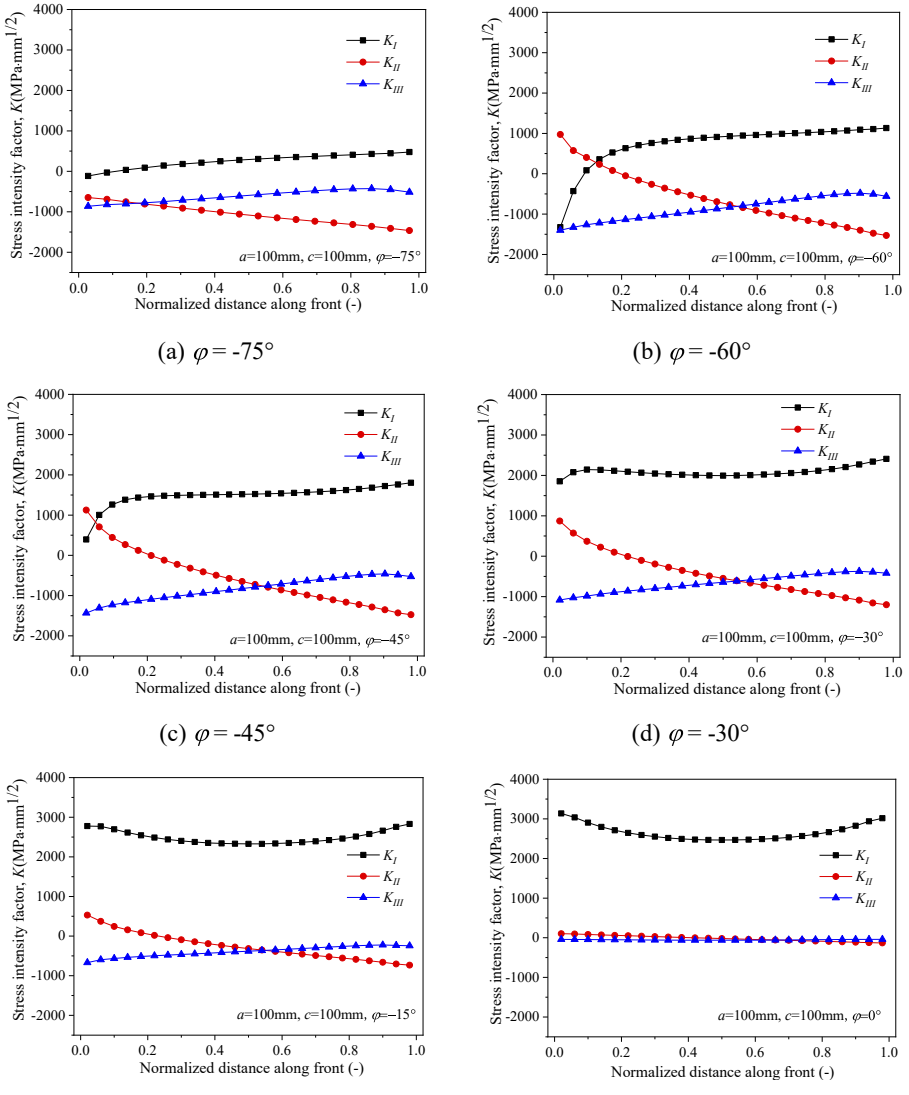

(a) φ = -75° (b) φ = -60°

(c) φ = -45° (d) φ = -30°

(e) φ = -15° (f) φ = 0°

Fig. 8. Results of stress intensity factor for S-03 (a = 100, c = 100).

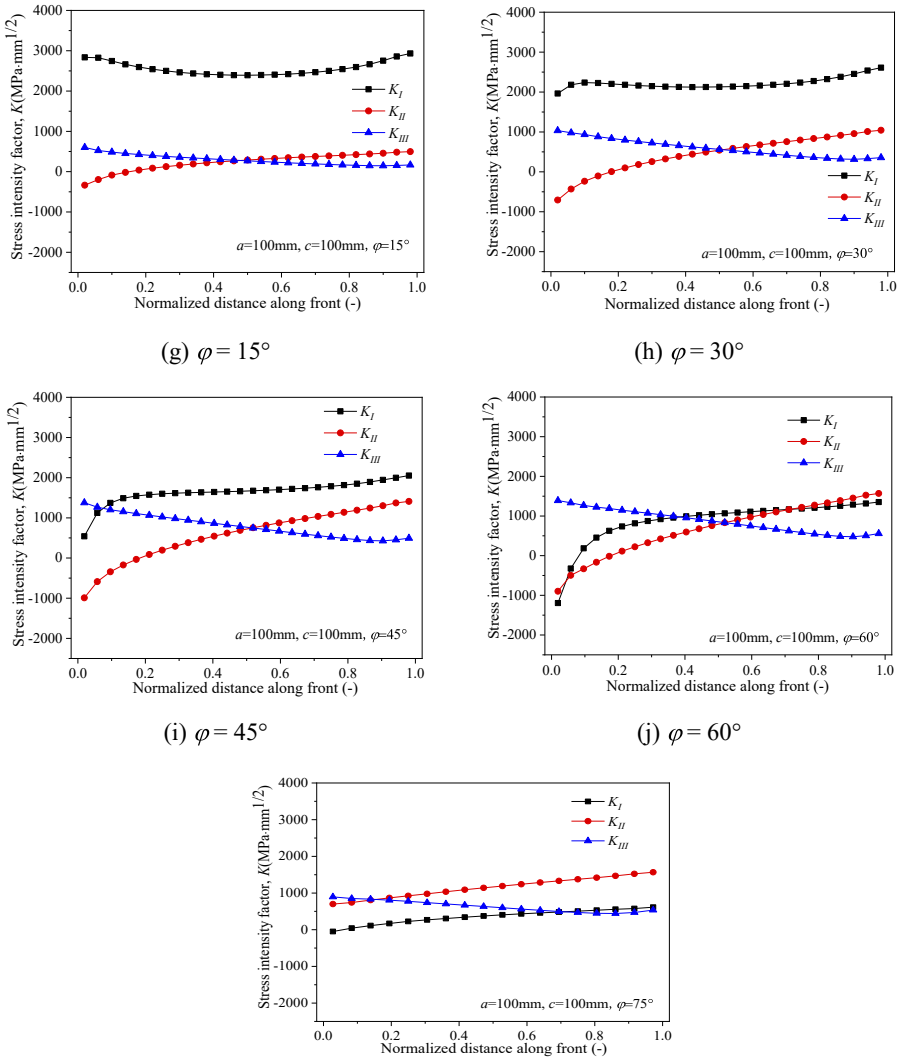

(g) $\varphi = 15°$ (h) $\varphi = 30°$

(i) $\varphi = 45°$ (j) $\varphi = 60°$

Fig. 8. (*continued*).

profile also shows a plateau when the corner crack angles are from −45° to 45° (M−shape with the local plateau). One of possible causes for the difference is that the SIF-based calculation lacks consideration of plastic effect of the material, and the *J* integral developed by Cherepanov and Rice is more appropriate to calculate the crack driving force with non-negligible plastic deformation (Cherepanov, 1967; Rice, 1968). It can be interpreted as that the K_{eff} (or K_I) have neglected the swift increase of crack driving force along the crack front when the crack angles are ±60°, while the *J* integral which is based on elastoplasic fracture mechanics theory can better describe the trend of crack growth.

4. Conclusions

A three-dimensional finite element analysis has been carried out on corner cracks in a RPV. The SIF and *J* integrals along the crack tip were calculated in terms of the crack depths, lengths and angles. Main conclusions are as follows:

(1) The highest stress concentration point of the RPV can be found at the intersection area between the set-in nozzle-cylinder and the inner wall.

(2) Slant corner crack in RPV are not just only affected by tensile mode crack (mode I), but also by sliding mode crack (mode II) or tearing mode crack (mode III). K_{II} and K_{III} should be taken into account in the structural integrity analysis of RPV.

(3) The location of the highest *J* or *K* is not fixed but varies, depending on the depth, length and angles of corner crack. The vertical corner crack has the highest *K* value while the corner crack with ± 60° has the local maximum *J* value.

(4) The K_{eff} (or K_I) cannot pick up the swift increase of crack driving force along the crack front when the crack angle is ± 60°, while the *J* integral which is based on elastoplasic fracture mechanics theory can better describe the trend of crack growth.

For purpose of structural integrity analyses of key nuclear structure such as RPV, many scholars and research institutions are taking efforts to predict the crack growth behaviour. Comparisons between the SIF and *J* solution from FEA may help to achieve this purpose by providing a better understanding on the prediction of the crack driving force.

CRediT authorship contribution statement

Shuai Wang: Investigation, Formal analysis, Data curation,

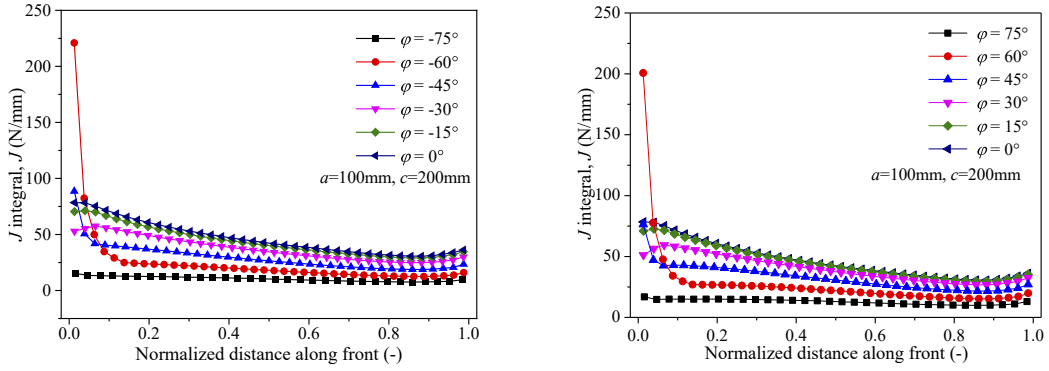

(a) $\varphi = -75° \sim 0°$ (b) $\varphi = 0° \sim 75°$

Fig. 9. J of the corner cracks of set No.S-01 ($a = 100$, $c = 200$).

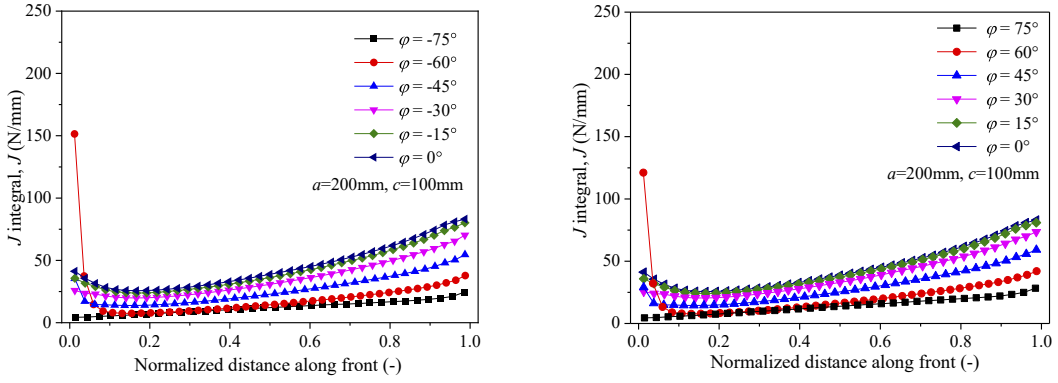

(a) $\varphi = -75° \sim 0°$ (b) $\varphi = 0° \sim 75°$

Fig. 10. J of the corner cracks of set No.S-02 ($a = 200$, $c = 100$).

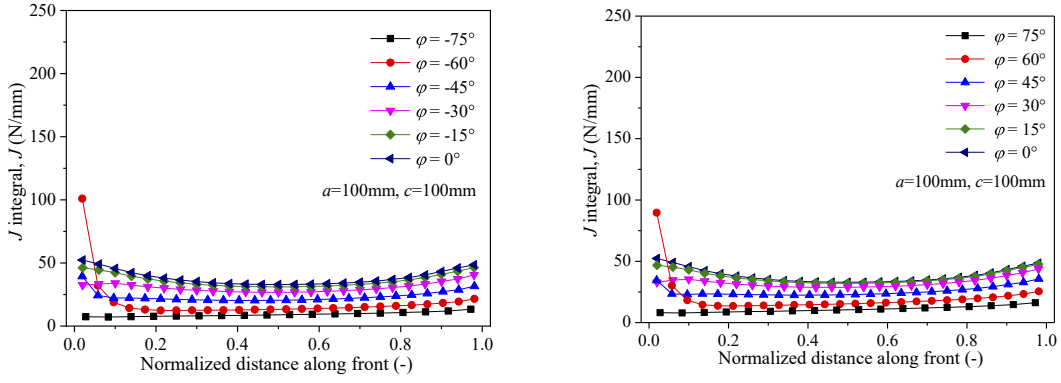

(a) $\varphi = -75° \sim 0°$ (b) $\varphi = 0° \sim 75°$

Fig. 11. J of the corner cracks of set No.S-03 ($a = 100$, $c = 100$).

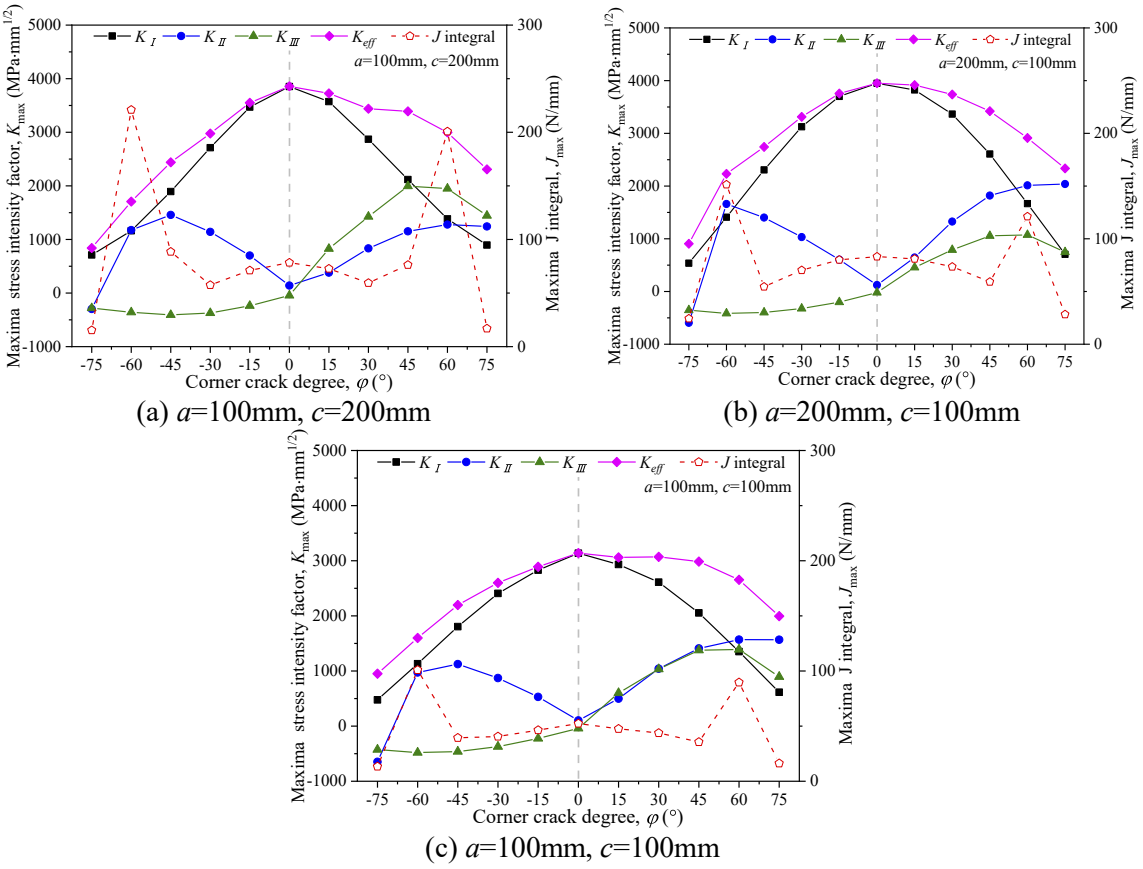

Fig. 12. The relationship between maximum J, K, φ and crack shape.

Validation, Software, Writing – original draft. **Bin Wang:** Project administration, Conceptualization, Methodology, Supervision, Funding acquisition, Writing – review & editing. **Guiyi Wu:** Supervision, Writing – review & editing, Project administration. **He Xue:** Funding acquisition, Validation. **Yuman Sun:** Data curation, Validation. **Jiajun Zhu:** Data curation.

Declaration of Competing Interest

The authors declare that they have no known competing financial interests or personal relationships that could have appeared to influence the work reported in this paper.

Data availability

Data will be made available on request.

Acknowledgements

This work was financially supported by the Guangdong Major Project of Fundamental and Applied Fundamental Research, China (2019B030302011), International Exchanges Programme Scheme project jointly by the Royal Society, UK (IEC\NSFC\170551) and National Natural Science Foundation, China (51811530311), Xi'an Jiaotong University State Key Lab for Strengths and Vibration for Mechanical Structures Open Lab Project, China (SV2017-KF-25), China Postdoctoral Science Foundation, China (2022MD723825), Natural Science Basic Research Plan in Shaanxi Province, China (2023-JC-QN-0474).

References

ABAQUS/Standard User's Manual, 2018. Dassault Systèmes Simulia Corp. Providence, RI, USA.

Banks-Sills, L., Hershkovitz, I., Wawrzynek, P.A., Eliasi, R., Ingraffea, A.R., 2005. Methods for calculating stress intensity factors in anisotropic materials: Part I—z=0 is a symmetric plane. Eng. Fract. Mech. 72, 2328–2358. https://doi.org/10.1016/j.engfracmech.2004.12.007.

Banks-Sills, L., Wawrzynek, P.A., Carter, B., Ingraffea, A.R., Hershkovitz, I., 2007. Methods for calculating stress intensity factors in anisotropic materials: Part II—Arbitrary geometry. Eng. Fract. Mech. 74, 1293–1307. https://doi.org/10.1016/j.engfracmech.2006.07.005.

British Energy, Assessment of the Integrity of Structures Containing Defects. British Energy Generation Report R6 Revision, 4, Gloucester, 2001.

BS7910:2019, 2019. Guide to methods for assessing the acceptability of flaws in metallic structures. British Standards Institution, London.

Cherepanov, G.P., 1967. Crack propagation in continuous media. J. Appl. Math. Mech. 31, 503–512. https://doi.org/10.1016/0021-8928(67)90034-2.

Dong, L., Peng, Q., Xue, H., Han, E.H., Ke, W., Wang, L., 2018. Correlation of microstructure and stress corrosion cracking initiation behaviour of the fusion boundary region in a SA508 Cl. 3-Alloy 52M dissimilar weld joint in primary pressurized water reactor environment. Corros. Sci. 132, 9–20. https://doi.org/10.1016/j.corsci.2017.12.011.

Jin, T., Wang, Z., Wang, Q., Wang, D., Li, Y., Zhou, M., 2019. Weibull stress analysis for the corner crack in reactor pressure vessel nozzle. Adv. Mech. Eng. 11 https://doi.org/10.1177/1687814019893567, 168781401989356.

Kim, J.-S., Seo, J.-M., Kang, J.-Y., Jang, Y.-Y., Lee, Y.-J., Kim, K.-W., 2022. Constraint-corrected fracture mechanics analysis of nozzle crotch corners in pressurized water reactors. Nucl. Eng. Technol. 54, 1726–1746. https://doi.org/10.1016/j.net.2021.11.022.

Li, Y., Jin, T., Wang, Z., Wang, D., 2020. Engineering critical assessment of RPV with nozzle corner cracks under pressurized thermal shocks. Nucl. Eng. Technol. 52, 2638–2651. https://doi.org/10.1016/j.net.2020.04.019.

Li, X., Song, Y., Ding, Z., Bao, S., Gao, Z., 2018. A modified correlation between KJIC and Charpy V-notch impact energy of Chinese SA508-III steel at the upper shelf. J. Nucl. Mater. 505, 22–29. https://doi.org/10.1016/j.jnucmat.2018.03.056.

Liu, R., Huang, M., Peng, Y., Wen, H., Huang, J., Ruan, C., Ma, H., Li, Q., 2018. Analysis for crack growth regularities in the nozzle-cylinder intersection area of Reactor Pressure Vessel. Ann. Nucl. Energy 112, 779–793. https://doi.org/10.1016/j.anucene.2017.10.021.

Liu, K., Huang, M., Lin, J., Jiang, H., Wang, B., Matsuda, H., 2020. The effects of thermal stress on the crack propagation in AP1000 reactor pressure vessel, 102798 Theor. Appl. Fract. Mech. 110. https://doi.org/10.1016/j.tafmec.2020.102798.

Liu, C., Jiao, G., Chandwani, R., Timbrell, C., 2021. Study on application range of SIF calculation method for nozzle corner crack in pressure vessel for ASME XI code. Int. J. Press. Vessels Pip. 193, 104478 https://doi.org/10.1016/j.ijpvp.2021.104478.

Murtaza, U.T., Hyder, M.J., 2015a. Optimization of the size and shape of the set-in nozzle for a PWR reactor pressure vessel. Nucl. Eng. Des. 284, 219–227. https://doi.org/10.1016/j.nucengdes.2014.12.040.

Murtaza, U.T., Hyder, M.J., 2015b. The effects of thermal stresses on the elliptical surface cracks in PWR reactor pressure vessel. Theor. Appl. Fract. Mech. 75, 124–136. https://doi.org/10.1016/j.tafmec.2014.12.001.

Murtaza, U.T., Hyder, M.J., 2017. Stress intensity factors of corner cracks at set-in nozzle–cylinder intersection of a PWR reactor pressure vessel. J. Braz. Soc. Mech. Sci. Eng. 39, 601–611. https://doi.org/10.1007/s40430-016-0522-x.

Okonkwo, B.O., Ming, H., Wang, J., Meng, F., Xu, X., Han, E.-H., 2021. Microstructural characterization of low alloy steel A508–309/308L stainless steel dissimilar weld metals. Int. J. Press. Vessels Pip. 190, 104297 https://doi.org/10.1016/j.ijpvp.2020.104297.

Qibao, C., Qing, W., Yonggang, F., Wei, T., 2022. Fracture assessment for pressurized water reactor vessel nozzles subjected to pressure and thermal loading, 051302 J. Press. Vessel Technol. 144. https://doi.org/10.1115/1.4053225.

Rice, J.R., 1968. A path independent integral and the approximate analysis of strain concentration by notches and cracks. J. Appl. Mech. 35, 379–386. https://doi.org/10.1115/1.3601206.

Ruiz, C., 1973. Stress intensity factors for nozzle corner cracks. Strain 9, 7–10. https://doi.org/10.1111/j.1475-1305.1973.tb01791.x.

Sun, X., Chai, G., Bao, Y., 2017. Elastic and elastoplastic fracture analysis of a reactor pressure vessel under pressurized thermal shock loading. Eur. J. Mech. - A Solids 66, 69–78. https://doi.org/10.1016/j.euromechsol.2017.06.008.

Sun, X., Yao, J., Chai, G., Bao, Y., 2019. Thickness effects of base wall and inlet pipe on the structural integrity of reactor pressure vessels considering ductile-to-brittle transition. Eng. Fail. Anal. 105, 1032–1044. https://doi.org/10.1016/j.engfailanal.2019.05.036.

Thamaraiselvi, K., Vishnuvardhan, S., 2020. Fracture studies on reactor pressure vessel subjected to pressurised thermal shock: A review. Nucl. Eng. Des. 360, 110471 https://doi.org/10.1016/j.nucengdes.2019.110471.

Tian, J., Fu, X., Shao, X., Jiang, L., Li, J., Kan, Q., 2020. Damage-coupled ratcheting behaviors of SA508 Gr.3 steel at room and elevated temperatures: Experiments and simulations. Int. J. Damage Mech. 29, 1379–1396. https://doi.org/10.1177/1056789520930406.

Wang, S., Wang, B., Janin, Y., Bourga, R., Xue, H., 2021. Effects of the surface crack shape on *J* values along the front of an elliptical crack. Fatigue Fract. Eng. Mater. Struct. 44, 2944–2961. https://doi.org/10.1111/ffe.13522.

Wang, S., Hou, C., Wang, B., Wu, G., Fan, X., Xue, H., 2022. Mechanical responses of L450 steel under biaxial loading in the presence of the stress discontinuity. Int. J. Press. Vessels Pip. 198, 104662 https://doi.org/10.1016/j.ijpvp.2022.104662.

Wang, S., Xue, H., Wu, G., Wang, Z., Zhao, K., Ni, C., 2023. Investigation of the Inhomogeneous Mechanical and Crack Driving Force of Low Alloy Steel SA508 and Its Welded 309L/308L Stainless Steel Cladding. Nucl. Sci. Eng. 197, 623–632. https://doi.org/10.1080/00295639.2022.2123210.

Yau, J.F., Wang, S.S., Corten, H.T., 1980. A Mixed-Mode Crack Analysis of Isotropic Solids Using Conservation Laws of Elasticity. J. Appl. Mech. 47, 335–341. https://doi.org/10.1115/1.3153665.

Zhang, X., Li, L., Qi, X., Zheng, J., Zhang, X., Chen, B., Feng, J., Duan, S., 2017. Experimental and numerical investigation of fatigue crack growth in the cracked gear tooth: Fatigue Crack Growth in the Cracked Gear Tooth. Fatigue Fract. Eng. Mater. Struct. 40, 1037–1047. https://doi.org/10.1111/ffe.12557.